

<https://doi.org/10.1038/s41528-024-00326-y>

Stabilizing Schottky junction in conjugated polymer diodes enables long-term reliable radio-frequency energy harvesting on plastic



Yongwoo Lee¹, Boseok Kang², Sungjune Jung³✉ & Jimin Kwon¹✉

Due to their inherent flexibility, solution-processable conjugated polymers are increasingly being considered for the cost-effective production of thin-film semiconductor devices used in Internet of Everything (IoE) applications. With considerable improvements in charge carrier mobilities, the final challenge impeding the commercialization of conjugated polymers may be improving their environmental and electrical stabilities. Recent studies have improved the stability of computing devices (i.e., transistors) by eliminating interface traps and water molecules within conjugated polymers. However, the stability issue of Schottky diodes, which play a crucial role in configuring thin-film IoE devices used in wireless communication and energy harvesting, has been largely overlooked. This study reveals that aluminum, which is commonly used as a cathode metal in polymer Schottky diodes, creates a nonstoichiometric effect when deposited on conjugated polymers, thereby leading to the formation of charge traps over time, which reduces the rectification ratio of the Schottky diodes and induces a significant bias stress effect during operation. To address this issue, we introduce a zinc-oxide sacrificial interlayer between the conjugated polymer and cathode. This interlayer effectively eliminates the penetrated Al metal or ionized Al-induced nonstoichiometric effect without reducing the charge injection efficiency, achieving exceptional environmental and operational stability. The printed polymer Schottky diodes demonstrate consistent rectifying operation at 13.56 MHz for several months with negligible changes in electrical characteristics.

Thin film electronics based on solution-processable semiconductors combined with printing techniques offer a facile way to manufacture wearable devices for digital healthcare monitoring^{1–3}, flexible information display^{4,5}, biomarker detection⁶, electronic skin^{7,8}, and brain signal recording^{9,10}. Inherently flexible conjugated polymers with moderate carrier mobilities outperform other high-carrier mobility semiconductor materials (e.g., oxide semiconductors, perovskites, and low-dimensional semiconductor dispersions) in specific wearable applications undergoing extreme mechanical deformation¹¹. Recent achievements have demonstrated that conjugated polymers can enable even more complex and intelligent computing devices with process scalability and systematic approaches on ultrathin flexible or stretchable substrates¹².

When configuring lightweight wearable devices, flexible circuit components must be used in all building blocks for logic, memory, display, and communication^{13–17}. To fully achieve a soft form factor, wearable devices must be powered using wireless energy harvesting technology rather than a hard energy storage component (i.e., battery). A conjugated polymer Schottky diode with a very low forward voltage drop can rectify the radio frequency (RF) energy efficiently, thereby converting the alternating current (AC; primarily at a frequency of 13.56 MHz) from the antenna into direct current (DC) to power a load^{18–22}. Note that these power switches require a high rectification ratio (RR), high switching speed, and more stringent operational stability than other circuit components because large currents flow continuously through the diodes when the device is on.

¹Departemnt of Electrical Engineering, Ulsan National Institute of Science and Technology (UNIST), 50 UNIST-Gil, Ulsan, 44919, Republic of Korea. ²SKKU Advanced Institute of Nanotechnology (SAINT), Department of Nano Science and Technology, and Department of Nano Engineering, Sungkyunkwan University (SKKU), Suwon, 16419, Republic of Korea. ³Departemnt of Materials Science and Engineering, Pohang University of Science and Technology (POSTECH), 77 Cheongam-Ro, Pohang, 37673, Republic of Korea. ✉e-mail: sjjung@postech.ac.kr; jmkwon@unist.ac.kr

The electrical characteristics of conjugated polymer Schottky diodes can deteriorate over time due to a combination of various environmental and material factors, and recent studies have focused on enhancing the operational stability of conjugated polymer devices. For example, atmospheric moisture can limit the charge transport in low-disorder conjugated polymers by increasing the trap density in the bulk semiconductor²³. In addition, exposure to air can result in oxidation and interfacial reactions of metal electrodes, e.g., Al and Ag, thereby reducing the Schottky barrier height and increasing the reverse current^{24,25}. Water-induced defects can be reduced dramatically by incorporating small molecular additives into polymer films to achieve trap-free space charge-limiting current characteristics in Schottky diodes²⁶, and proper encapsulation of the device can prevent the ingress of oxygen, water, and other environmental factors causing oxidation of the metal electrode^{27,28}.

However, the stability of the Schottky barrier junction between conjugated polymers and low-work function metals is not yet fully understood. In this study, we reveal an intrinsic instability caused during the formation of low-work function metal. Note that Al has been widely utilized as a cathode material for conjugated polymer Schottky diodes due to its low work function and good process compatibility²⁹. The work function of Al is located near the middle of the bandgap of most p-type conjugated polymers; the HOMO and LUMO values range from -5.0 to -5.5 eV and -2.7 to -3.7 eV, respectively^{30,31}. The Al and conjugated polymer contact barrier makes charge injection difficult in both directions, forming an ideal Schottky junction. However, the use of Al can lead to oxidation and non-stoichiometric compounds at the metal-semiconductor interface over time, which results in a gradual degradation of the RR and causes severe bias stress effects during operation^{18,32,33}. Due to device stability issues, many studies have evaluated the diode characteristics in inert environments without moisture and oxygen; however, ambient and inert environments can cause significant differences in the charge injection and contact barrier at the interface between the metal and organic semiconductor (OSC)³⁴. Thus, the stability and reliability of organic Schottky diodes must be enhanced based on an understanding of the contact barriers between low-work function metals and conjugated polymers.

In this paper, we demonstrate a highly stable conjugated polymer Schottky diode that can rectify 13.56 MHz signals for a few months without degradation by addressing a critical instability issue in the polymer-metal interface. First, we represent that the origin of rapid current degradation of diodes immediately after fabrication is primarily due to the Al-cathode-mediated doping effect rather than the oxidation of the semiconductor or cathode. The doped behavior of the polymer OSC is observed physically using X-ray photoelectron spectroscopy (XPS) and analyzed electrically using organic field-effect transistors. To prevent cathode doping, we utilize a few nanometers of a zinc-oxide (ZnO) interlayer between the conjugated polymer and cathode, which has a work function value similar to that of Al. This approach eliminates oxygen vacancies and reduces electrical traps, thereby maintaining charge injection efficiency and achieving remarkable environmental and operational stabilities. The printed polymer Schottky diodes exhibit stable and reliable rectifying over several months, demonstrating a full-wave rectifier operating at 13.56 MHz.

Results

Rapid performance degradation of polymer Schottky diodes

Rectifying thin film diodes are essential for energy harvesting in standalone flexible electronics in the radio-frequency electromagnetic field (Fig. 1a). Polymer Schottky diodes comprising Au bottom metal, conjugated polymer active layer, and Al top metal were fabricated on a 1- μm thick parylene film (Fig. 1b, c). Here, thermally evaporated Au (100 nm) and Al (50 nm) electrodes serve as the anode and cathode, respectively, and the p-type semiconductor, i.e., Poly[3,6-bis(5-thiophen-2-yl)-2,5-bis(2-octyldodecyl)pyrrolo[3,4-c]pyrrole1,4(2H,5H)-dione-2,2'-diyl-alt-thieno[3,2-b]thiophen-2,5-diyl] (DPP-DTT; Fig. 1d) was printed using a dispenser (250–500 nm). The donor-acceptor-type copolymeric system of DPP-DTT offers features such as solution processability, chemical stability, and high mobility, which

facilitate printing processes in ambient air conditions^{35,36}. The fabrication process is described in detail in the Methods section. The flexible rectifying antenna can directly convert electromagnetic energy in the form of AC to DC electricity, thereby providing power to a load that is connected to its output. This can be realized by restricting the current flow exclusively in one direction, governed by the energy level alignment between the semiconductor and the metal. The Schottky barrier height (Φ_B) is determined at the junction of a metal/organic p-type semiconductor interface after the free charge carriers in the OSCs transfer to align the fermi level (E_F) of the OSC with the work function of the metal (Φ_M) (Fig. 1e). Φ_B is calculated as the difference between the highest occupied molecular orbital (HOMO) level of the organic material and Φ_M .

Given that the rectification characteristic of the Schottky diode plays a critical role in terms of determining its conversion efficiency, it is imperative that the rectifying barrier height between the metal and semiconductor at both the anode and cathode is designed carefully. In addition, scaling the high-frequency characteristic of rectifiers is closely related to the charge transport of an OSC/metal Schottky diode, with the primary determinant being the forward current density. Therefore, achieving stable and continuous operation of the diode over an extended period is of significant importance. However, as shown in Fig. 1f, a reduction in performance was observed after the fabrication of the Schottky diode, with a decline in forward current and an increase in reverse current, which resulted in an approximately 300-fold decrease in the RR after 96 hours of storage in a dry ambient environment (20 °C, 0% relative humidity, RH). The degradation phenomenon occurred rapidly over a one-day period, and after 7 days, the RR gradually reached a value of 480. Note that the instability of the polymer diode ultimately hinders its ability to harvest energy effectively because a degradation in the forward current value leads to a decline in the efficiency of converting AC power into DC diode voltage (V_D). The rectified V_D is determined by the current recharging the load capacitance (C_L) with the charges consumed by the load (R_L) during a single frequency cycle (ω).

$$\frac{V_D}{R_L} \cdot \frac{2\pi}{\omega} = \int_{t_1}^{t_2} I_{\text{Forward}} dt \quad (1)$$

where t_1 and t_2 define the time interval during which the diode is in a forward bias state. Frequency measurements of the rectifier comprised 100 nF (C_L) and 10 M Ω (R_L). Compared with the immediate postfabrication, the performance of the rectifier was considerably poorer after seven days, with the output power voltage decreasing by 28% at 1 kHz and 83% at 10 MHz (Fig. 1g).

The forward current density was degraded in both ambient and inert environments, as shown in Fig. 1h. Note that the deterioration of the electrical performance may also occur in environments with minimal water or oxygen in ambient air. To examine when degradation occurs, the device was fabricated up to only the OSC layer, and then the cathode was deposited at time intervals of 0, 2, and 4 days. Degradation was observed immediately from each moment when the Al was deposited on the OSC layer (Fig. 1i). We observed that the forward current density began to decrease, and the reverse current density increased in an ambient environment. The corresponding $J_D - V_D$ curves over time are shown in Supplementary Fig. 1. Each current density measured shortly after completion of device fabrication (0, 2, and 4 days) exhibited high similarity, which suggests that the rapid RR reduction is likely due to degradation at the interface between the OSC layer and the cathode rather than degradation of the organic active layer.

Origin of rapid current degradation of diodes

It is possible that the instability of diodes can be attributed to the doping effect of the Al cathode. Figure 2a presents a schematic depiction of the degradation mechanism wherein thermally evaporated Al diffuses into the semiconductor. Note that metal diffusion into the OSC layer has been observed previously^{37–39}. Moreover, the deposition of a cathode material with high specific gravity, e.g., Ag (approximately 10.5), facilitates penetration of the metal into the semiconductor. The nonlinear $J_D - V_D$

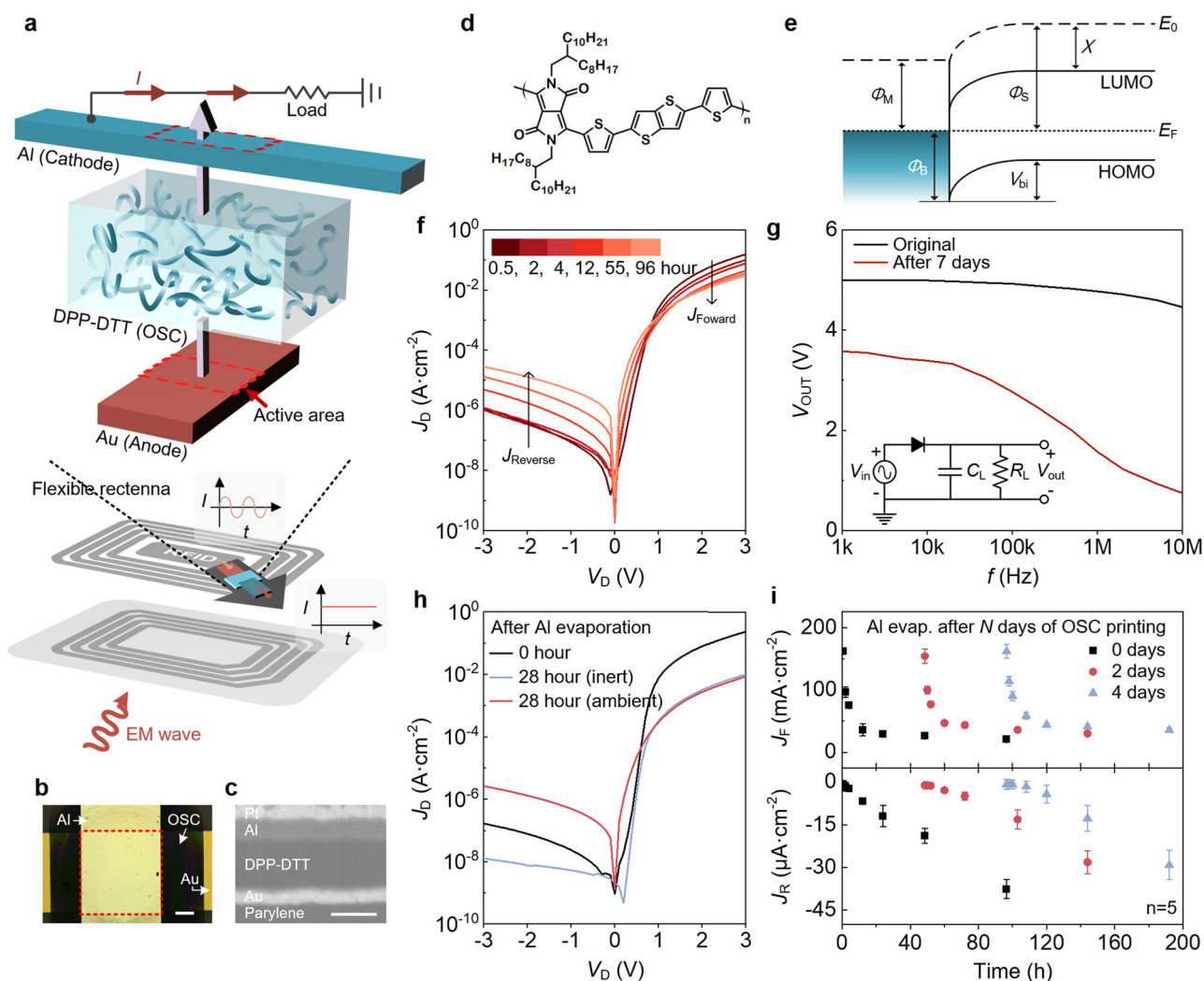


Fig. 1 | Polymer Schottky diodes for energy harvesting and their stability issues.

a Schematic of an energy harvesting system with a flexible antenna and rectifiers. The inset shows the top view of the schematic. **b** Optical image of the diode. The red dotted line indicates an active area of a diode (the scale bar is 200 μm). **c** Scanning electron microscope image of the Au/DPP-DTT/Al Schottky diode (the scale bar is 100 nm). **d** Chemical structure of DPP-DTT. **e** Energy band diagram of Schottky contact between cathode and organic semiconductor. **f** $J_D - V_D$ characteristics as a

function of storage time of the printed polymer DPP-DTT diodes. **g** Frequency response of the DPP-DTT rectifier before and after degradation. The inset shows the rectifier circuit diagram. **h** Changes in $J_D - V_D$ characteristics of the DPP-DTT diode over time in inert and ambient air environments. **i** Changes in forward and reverse current density over time after Al cathode deposition. Al was deposited 0, 2, and 4 days after the organic semiconductor layer was fabricated (the error bars represent standard deviation).

characteristics of the diode immediately after deposition of the cathode material changed to ohmic characteristics over time, as shown in Supplementary Fig. 2. Due to its lower specific gravity (approximately 2.7), Al does not alter the diode characteristics significantly; however, during thermal evaporation, hot Al atoms with high kinetic energy can undergo slight diffusion into the OSC³⁸. When Al penetrates into an OSC layer, the Al metal can be oxidized inside the organic layer, and other Al atoms can remain ionized. The ionized Al, which may not have undergone complete oxidation, can potentially allow for hybridization between the remaining dangling bonds of AlO_x and the orbitals of the OSC. This hybridization can potentially serve a donor role within the OSC.

To investigate the effect of penetrated Al on the OSC layer, XPS measurements were performed. Here, to examine the material composition at the interface between Al and OSC, XPS depth profiles were measured in conjunction with an Ar^+ etching process. The etching rate was approximately 0.2 nm s^{-1} . Figure 2b shows the XPS spectra of Al 2p and O 1s peaks at the metal, OSC, and interface. The XPS data were extracted from the data obtained through XPS depth profiles of the diode (Supplementary Fig. 3) at the metal layer (32 nm), interface (98 nm), and OSC (138 nm). The Al 2p

spectrum may be deconvoluted into two peaks with binding energies of 72.2 eV (Al metal) and 74.8 eV (Al oxide), and we confirmed that 51.8% of the Al metal remained unoxidized at the interface area. The O 1s spectra of the interface area were also deconvoluted to obtain two peaks at 532 eV (O_{VAC}) and 530.5 eV (O_M), indicating an oxygen-deficient region and oxygen-bonded region based on stoichiometry. Note that an absent atom does not produce signals in the XPS spectra; however, the presence of an atypical signal from an existing atom can be used as an indirect indicator of the percentage of the absent atom⁴⁰. The oxygen vacancy, i.e., the presence of unbonded oxygen molecules, was 38.6% of O 1s. The nonstoichiometric effect caused by the dangling bonds of the Al metal or Al oxides that have penetrated into the OSC layer can cause electrical traps, which function as charge-trapping centers and reduce the charge carrier transport efficiency. These factors cause electrical performance degradation of the diodes in which the forward current density decreases rapidly.

The influence of the degradation process on the interfacial band alignment is shown in Fig. 2c and d. When an anode metal contacts a semiconductor, the work function of the metal and the Fermi level of the semiconductor are forced to align such that band bending occurs and the

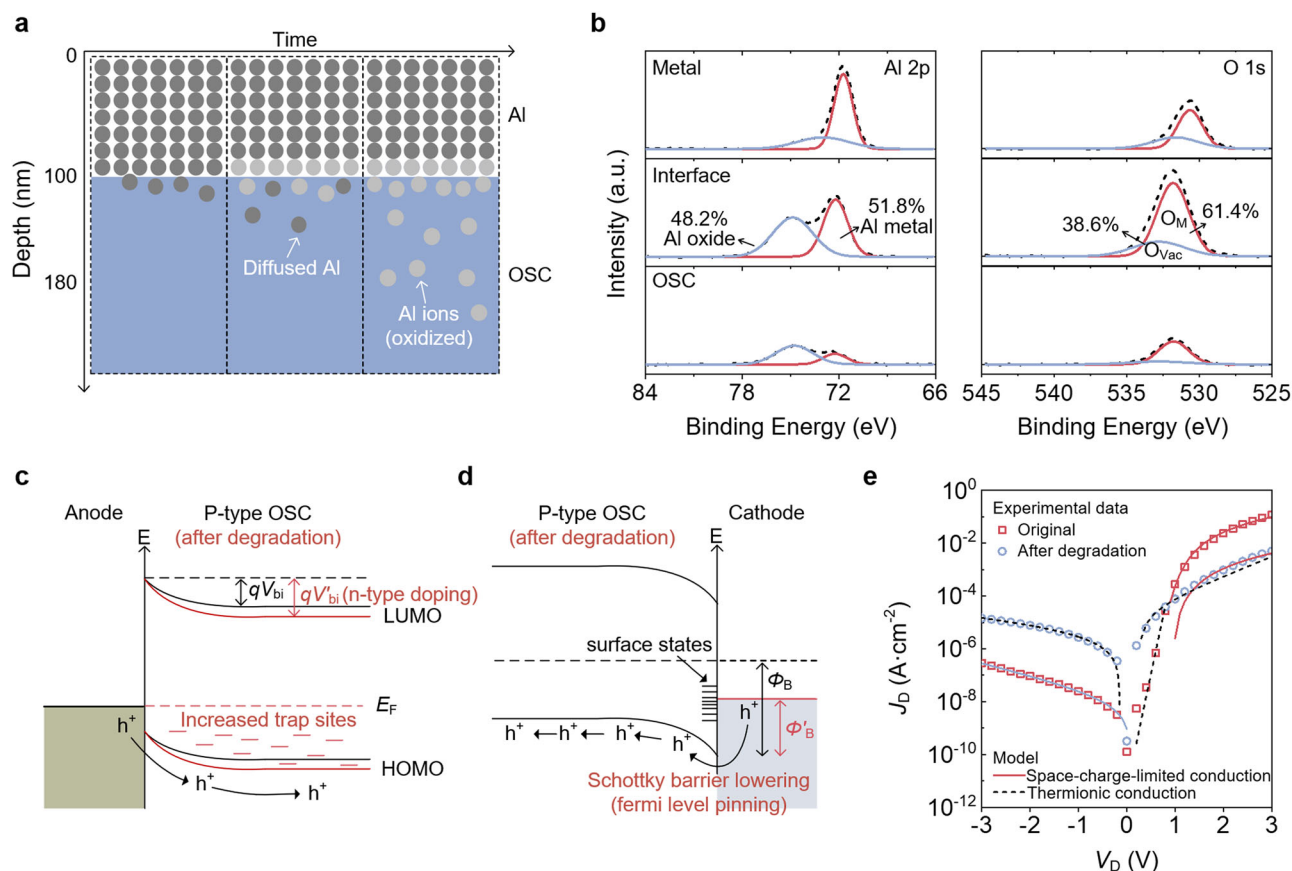


Fig. 2 | Degradation mechanism. **a** Schematic of the temporal evolution of Al deposited on p-type OSC. **b** Al 2p and O 1s XPS data at the metal, interface, and OSC layer of the DPP-DTT diode. **c, d** Energy band diagram of metal-p-type OSC contact

at ohmic and Schottky junction over time, respectively. **e** J_D - V_D characteristics of polymer DPP-DTT diodes before and after degradation.

Schottky barrier height is determined. Due to the low carrier density in p-type OSCs, the Fermi level was positioned slightly below the midpoint between the HOMO and the lowest unoccupied molecular orbital (LUMO). The DPP-DTT has a bandgap of 1.7 eV, with HOMO and LUMO levels at -5.2 eV and -3.5 eV, respectively³⁶. Here, the Fermi level of p-type OSC shifts toward the LUMO level by the influence of the Al-cathode-mediated doping, which results in a higher built-in potential (Fig. 2c). As a result, a higher voltage is required to achieve the same current density, thereby resulting in a significant reduction in the forward current density. The presence of a native oxide layer on the buried interface of the Al cathode can function as an interfacial dipole at the interface, which can also facilitate the Fermi level pinning, which in turn leads to a reduction in the Schottky barrier height (Fig. 2d).

These charges can also result in a leakage current path, which can induce the Ohmic property in the low forward bias region and an increase in the reverse current density over time. After degradation, the J_D - V_D curve can be described as two phenomena that occur simultaneously while increasing the thermionic conduction current under reverse bias and reducing the space-charge limited current under forward bias (Fig. 2e). In the thermionic conduction model, electrons surmount the work function as a consequence of either thermal energy or an externally applied electric field, subsequently transitioning to the HOMO level of the OSC. The resultant current density is expressed as follows.

$$J_D = J_0 \exp\left(\frac{qV_D}{\eta kT}\right) = A^* T^2 \exp\left(\frac{-q\Phi_b}{kT}\right) \exp\left(\frac{qV_D}{\eta kT}\right) \quad (2)$$

Here, J_0 is the saturation current density, η is the ideal factor, q is the electronic charge, k is the Boltzmann constant, T is the absolute temperature, A^* is the Richardson constant, Φ_b is the Schottky barrier height, and V_D is the

applied voltage. The Schottky barrier height was extracted by employing a fitting procedure using the saturation current in Eq. (2). Note that the value of A^* is $120 \text{ A cm}^{-2} \text{ K}^{-2}$ for free electrons⁴¹. For the diodes immediately after fabrication and after degradation, the J_0 values were $1.26 \times 10^{-8} \text{ A cm}^{-2}$ and $6.35 \times 10^{-6} \text{ A cm}^{-2}$, respectively, and the Schottky barrier height values were 0.86 and 0.70 eV, respectively. The space charge limited conduction (SCLC) is dependent on the presence of trap states located in the polymer semiconductor and interfacial layer between the metal and the OSC. The SCLC current density equation follows the Mott-Gurney law⁴², i.e.,

$J_D = \frac{9}{8} \epsilon \epsilon_0 \mu \frac{V_D^2}{d^3}$, where ϵ is the dielectric constant, ϵ_0 is the permittivity of free space, μ denotes the carrier mobility, and d is the thickness of the OSC film. After degradation, the extracted mobility was reduced from $5.0 \times 10^{-3} \text{ cm}^2 \text{ V}^{-1} \text{ s}^{-1}$ to $2.1 \times 10^{-4} \text{ cm}^2 \text{ V}^{-1} \text{ s}^{-1}$. The mobility was derived from J_D - V_D curve and may differ from the mobility of the material itself. The presence of partially ionized Al can result in the formation of nonstoichiometric compounds that produce electrical trap sites, resulting in a major factor contributing to diode degradation.

Overcoming degradation for a stable Schottky diode

Adding an Al-doped ZnO (AZO) interlayer (several nanometers thick) between the conjugated polymer and cathode enables the filling of physical trap sites and compensation for the electrical traps (Fig. 3a). The interlayer serves as a buffer layer that can prevent direct contact between the two materials and eliminate the nonstoichiometric effect by forming a densely packed OSC. We confirmed the formation of AZO between the OSC and cathode via secondary ion mass spectroscopy data using the Al, C, O, and Zn markers for diodes with and without AZO interlayer, respectively (Fig. 3b). Visual evidence obtained from both atomic force microscopy and scanning electron microscopy images confirms the formation of AZO on the OSC

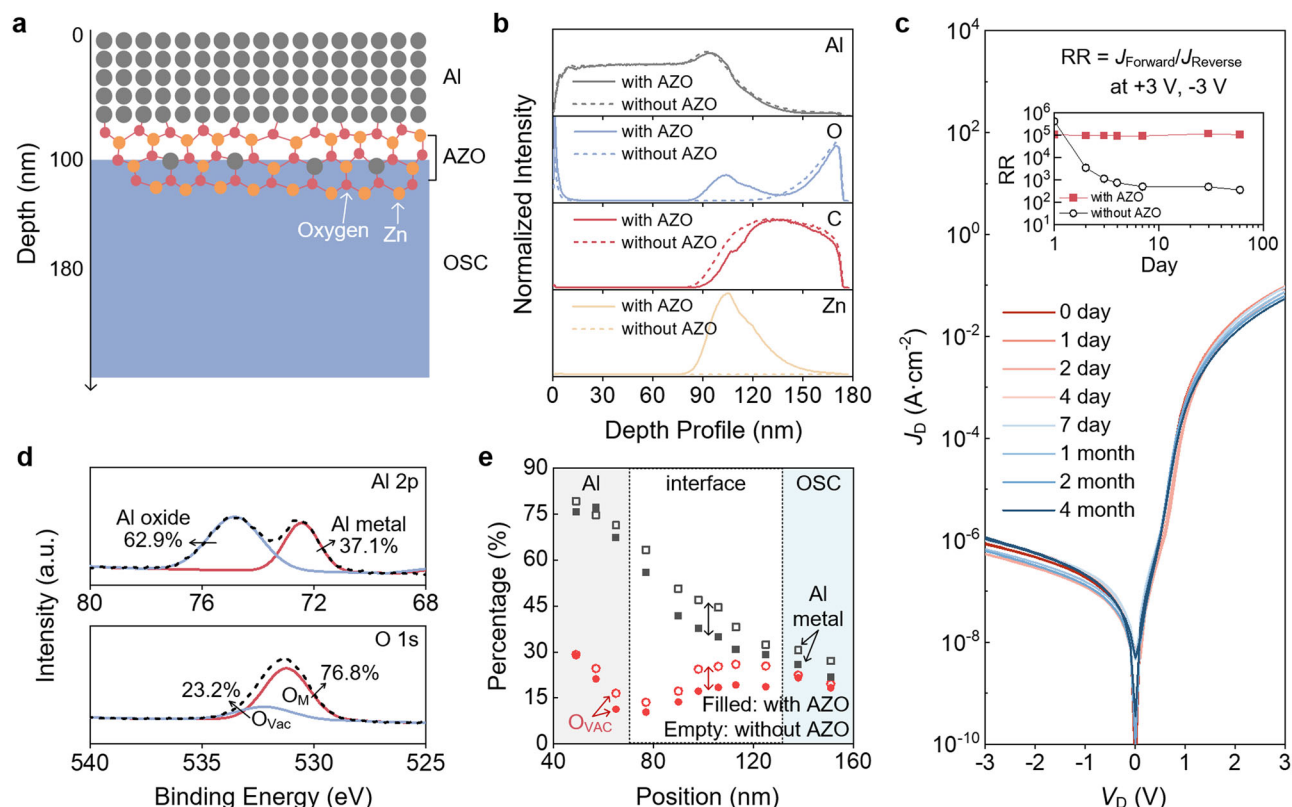


Fig. 3 | Stabilization of polymer Schottky diodes using an Al-doped ZnO interlayer. **a** Schematic of a stoichiometric aluminum oxide surface with Al-doped ZnO. **b** SIMS depth profiles of the DPP-DTT/Al (dashed line) and DPP-DTT/Al-doped ZnO/Al (solid line). **c** J_D - V_D characteristics as a function of storage time of DPP-DTT diodes with Al-doped ZnO interlayer (the inset shows the changes in

rectification ratio (RR) with and without an AZO interlayer over time). **d** Al 2p and O 1s XPS data of DPP-DTT diode with Al-doped ZnO interlayer. **e** Percentage of aluminum metal and oxygen vacancy (O_{vac}) as a function of depth with and without AZO interlayer corresponding to XPS results.

layer (Supplementary Fig. 4). Remarkably, devices with an AZO layer (Au/DPP-DTT/AZO/Al) exhibited long-term stable operation, maintaining an RR value of approximately 10^5 . Little change in electrical performance was observed when stored in ambient air for more than four months (Fig. 3c). The highly reliable mechanical stability of the diode is also presented in Supplementary Figs. 5 and 6. Among the solution-processed polymer OSC-Schottky diodes, the operation of this diode in ambient air demonstrated the best stability and superior performance (Supplementary Table 1). The thickness of the interlayer was optimized, as shown in Supplementary Fig. 7. While an excessively thick interlayer can exhibit less degradation compared to devices without an interlayer, these thicker layers can impact charge injection, leading to lower current density levels and an inability to fully prevent degradation. A thickness of approximately 10 nm or less was optimal to maintain a high rectification ratio and stable operation. Attempts to form a thinner layer by diluting the ink further hindered film formation and induced device degradation.

Figure 3d shows the change in the XPS intensity ratio of the Al 2p and O 1s peaks at the DPP-DTT/Al interface with and without the insertion of AZO. The Al oxide contents of Al 2p increased from 48.2% to 62.9%, which means that the influence of the Al ions (used to act as an n-type dopant) was insignificant. The estimated part of the $O_{vac}/(O_{vac} + O_M)$ of the diodes with an AZO interlayer decreased from 38.6% to 23.2% compared to the diodes without the interlayer. Supplementary Fig. 8 shows the XPS data for the depth profiles of the diode. Through the XPS results, obtained by layer-specific positioning of Al and OSC along the z-axis, it was confirmed that both the ratio of Al metal and oxygen vacancy decreased at the vicinity of the interfacial region (Fig. 3e). Thus, it is suggested that the oxygen deficiency was reduced due to the AZO, which prevents

structural degradation of the OSC. Penetration of the Al could potentially disrupt the crystal structure of the OSC, thereby leading to trap formation. In addition, the AZO insertion could minimize the interdiffusion region at the interface between the OSC and Al contact, which is caused by Al evaporation, thereby enhancing device stability.

Considering the energy band diagram, it appears that the presence of the AZO layer prevents the shifting of the fermi level of the OSC. Thus, the maintenance of the potential barrier height leads to no substantial variation in the forward current value. The charge transport under the forward bias is not influenced significantly by the interlayer because it is only a few nanometers thick. Note that the work function of the AZO solution is -4.3 eV, which is aligned appropriately with the Al cathode, which has a -4.28 eV work function. It appears that the interlayer reduces both the interfacial doping due to oxidation and the density of trap states at the interface, thereby preserving both the preexisting Schottky contact and reverse current.

Verification of Al doping effect using organic field-effect transistors

To confirm the electrostatic doping effect of the Al anode on the OSC layer, an organic field-effect transistor was fabricated based on the DPP-DTT semiconductor material. Here, to imitate the situation where Al is deposited on the OSC layer, a very thin Al (less than 1 nm) layer was thermally evaporated on the exposed DPP-DTT of the transistor having a bottom-gate, coplanar structure (Supplementary Fig. 9a). The diffused Al on top of the semiconductor acts as an n-type dopant; thus, the number of hole carriers accumulated in the channel of the transistor decreased, and the transfer characteristic curve shifted left (Supplementary Fig. 9b). The trap density in

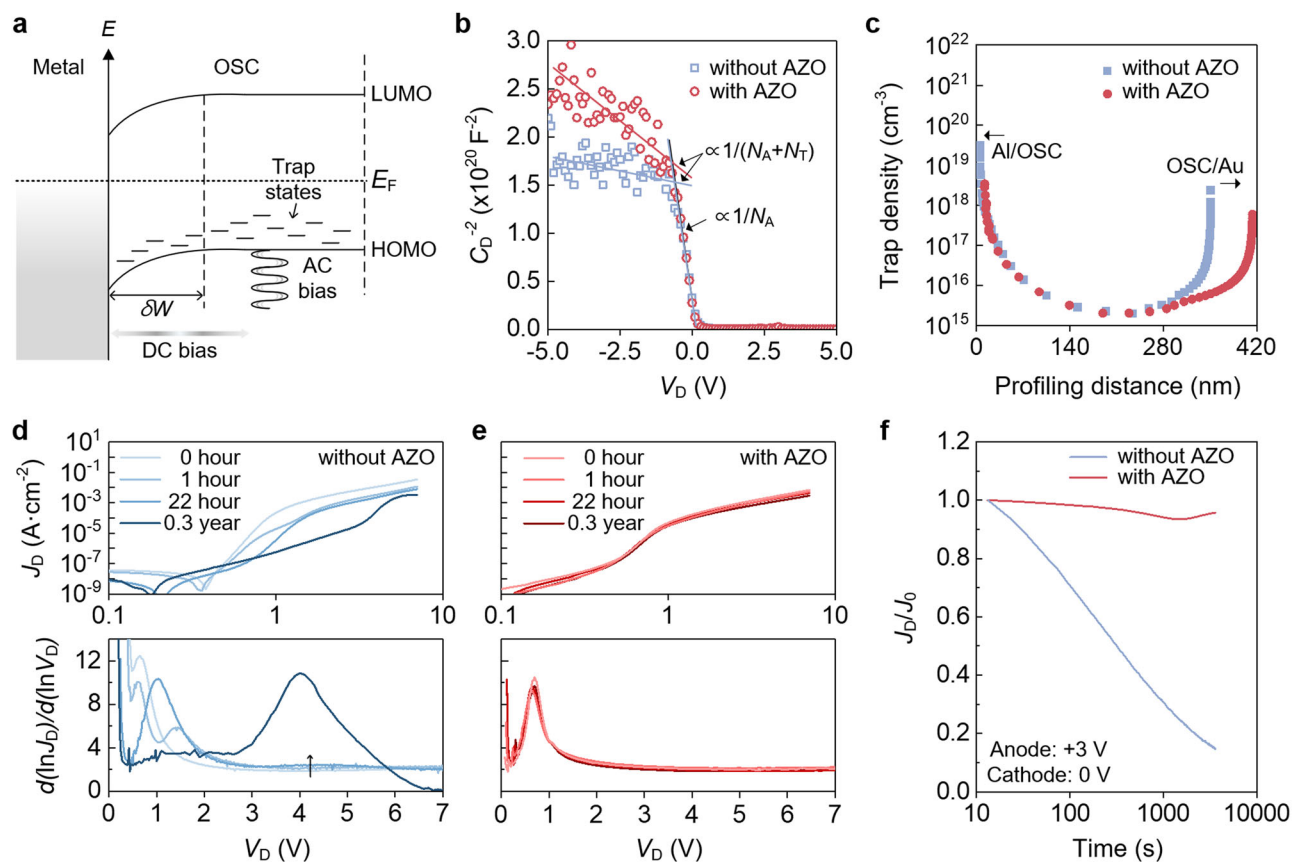


Fig. 4 | Analysis on electrical trap density and operational stability. **a** Schematic of band bending of metal-p-type OSC junction with trap states. **b** $C_D^{-2} - V_D$ characteristics of organic Schottky diodes with and without Al-doped ZnO interlayer (the solid line is fitted line by Eq. (4) for the extraction-free carrier and trap density). **c** Trap density as a function of profiling distance for DPP-DTT diode with and

without Al-doped ZnO interlayer measured at an AC frequency of 1 kHz. Log-log $J_D - V_D$ characteristics and corresponding power law exponent ($\partial \ln(J_D)/\partial \ln(V_D)$) of a DPP-TT diode (**d**) with and (**e**) without Al-doped ZnO interlayer. **f** Normalized current of DPP-DTT diodes with and without Al-doped ZnO interlayer after electrical bias stress for 3600 s.

organic field-effect transistors can be calculated as follows.

$$\Delta V_t = \frac{qN_{\text{trap}}}{C_i} \quad (3)$$

Here, V_t is the threshold voltage, q is the electronic charge, and C_i is the capacitance per unit area of the dielectric layer. With a parylene dielectric permittivity (ϵ) of 3.8 and a thickness (d) of 200 nm, the capacitance $C_i = \epsilon\epsilon_0/d$ was calculated as $1.68 \times 10^{-8} \text{ F}\cdot\text{cm}^{-2}$. The trap density was estimated to be approximately $2.63 \times 10^{11} \text{ cm}^{-2}$ without the additional layer over DPP-DTT. It appears that the electrostatic doping of the Al ions can be explained as a direct cause of the rapid reduction in the forward current of the organic Schottky diode. To verify the suppression of the electrostatic doping effect caused by adding the interlayer between the metal and the OSC, an AZO layer was added on top of the DPP-DTT. Note that the electrical characteristics of the DPP-DTT transistor before and after the formation of the AZO on the surface of the semiconductor by spin-coating are identical. Even though the Al deposition was conducted with the same protocol, there was little difference in both the transfer and linear characteristics of the transistors (Supplementary Fig. 9c), which implies that the interlayer can energetically prevent the shift of the Fermi level of the OSC. With the AZO interlayer, the trap density was further reduced to $4.41 \times 10^{10} \text{ cm}^{-2}$.

Analysis of electrical traps

A capacitance-voltage ($C_D - V_D$) measurement suggests that the AZO interlayer both slows the device degradation process and plays a key role in

reducing the electrical trap. Both the spatial and energetic distribution of defects can be obtained by changing the applied DC bias and varying the frequency of the AC bias, respectively (Fig. 4a). Note that this method assumes that a depletion layer is formed at the Schottky junction, which leads to an absence of free carriers in the space charge region; thus, all carriers found in the depletion layer arise from the defect state. The free carrier, trap density, and Schottky barrier height were determined by a $C_D^{-2} - V_D$ plot according to the following Mott-Schottky relation⁴³.

$$\frac{1}{C_D^2} = \frac{2}{A^2 q \epsilon \epsilon_0 N_A} (V_{bi} - V_D) \quad (4)$$

Here, C_D is the capacitance of a diode, A is the active area of a diode, ϵ is the permittivity of the semiconductor, ϵ_0 is the permittivity of free space, N_A is the density of carriers, q is the elementary charge, V_{bi} is the built-in potential, and V_D is the applied voltage. From the capacitance equation $C_D = \epsilon\epsilon_0 A/d$ and assuming fully depleted width under reverse bias, the permittivity of the DPP-DTT semiconductor was calculated to be approximately 3 (250 nm, 106 pF, $1 \times 1 \text{ mm}^2$). The gradient and x-intercepts of the linear fits to the capacitance measurement shown in Fig. 4b for two devices indicate the total carrier density and built-in potential, respectively. The deep trap density can be extracted qualitatively according to the difference between the two slopes⁴⁴. The slope of the near 0 V bias is related to the density of the shallow-level states ($1/N_A$), and the slope of the reverse bias is associated with the density of both the shallow-level states and the deep-level states ($1/(N_A + N_T)$). The fitting results were N_T of diodes without AZO interlayer = $6.73 \times 10^{16} \text{ cm}^{-3}$ and N_T of diodes with AZO interlayer = $2.13 \times 10^{16} \text{ cm}^{-3}$. To calculate the trap density quantitatively, a point-to-point $C - V_D$

measurement was conducted to yield the density of defect states at the distribution of states within the energy gap.

$$N(x) = -\frac{2}{A^2 q \epsilon_0} \frac{dV}{d(1/C_D^2)} \quad (5)$$

Here, x is the distance from the junction^{45,46}. The trap density as a function of spatial location by changing the depletion width is shown in Fig. 4c. The measured depletion charge density is in the order of 10^{15} – 10^{16} cm⁻³ in the mid-range and higher values of the trap density near both contacts. In particular, the diode without an interlayer has a high trap density near the Schottky contact due to the presence of deep-level trap states that do not contribute to the generation of free mobile charges. The trap density of the diode with the AZO interlayer at the Al/OSC interface was approximately 40 times less than that of the diode without an interlayer. The increase in trap density in the vicinity of the Schottky interface can enhance the electric field at the interface under reverse bias, which results in a reduction in the Schottky barrier width, and this has the potential to induce electron tunneling across the barrier. As a result, inserting the AZO layer can prevent such a phenomenon. In addition, electrochemical impedance spectroscopy can further clarify how the AZO interlayer stabilizes the electrical characteristics of the diodes. The impedances of the DPP-DTT diodes were measured in the range of 1 Hz to 10 MHz. The Nyquist plot of the diodes with the interlayer appears as if two semicircles have merged due to the formation of an extremely thin AZO layer. This is also confirmed by the shape of the graph of the diodes with the AZO interlayer consisting of two distinguishable semicircles at the forward bias condition (Supplementary Fig. 10). We found that the impedance shape of the diode without the interlayer changed over time. Here, the size of the circle indicates that the impedance value of the diodes increased and decreased under the forward and reverse bias conditions, respectively. The diodes with the interlayer exhibited little change in impedance over the measured frequency range and different voltage conditions regardless of the temporal variation.

The presence of traps can also be inferred through the slope of $\log J_D - \log V_D$. In Supplementary Fig. 11, the change of slope (m) in a log-log scale of $J_D - V_D$ characteristic shows that the type of charge transport, such as trap-free ($m = 2$), trap-filling ($m \gg 2$), ohmic ($m = 1$), follows Mott–Gurney law.

$$J_D = I_D/A = \frac{9}{8} \epsilon \epsilon_0 \mu \frac{V_D^m}{d^3} \quad (6)$$

Here, A is the active area of an organic diode, ϵ is the dielectric constant, ϵ_0 is the permittivity of free space, μ is the field-independent carrier mobility, V_D is the applied voltage, and d is the film thickness. Figure 4d and e show log-log plots of the $J_D - V_D$ characteristics for diodes with and without an interlayer, respectively. Due to more electrical traps, the diode without the AZO interlayer has a transition voltage greater than 0.1 V and several secondary peaks of slopes compared with the diode with the AZO interlayer. The trap concentration and their energy distribution shifted the height and voltage corresponding to the secondary trap peak. For the diode without the interlayer, an increase in the slope was observed over time in the extended plateau region between 3 V and 7 V, while for the diode with the interlayer, there was no significant change, and SCLC behavior was observed regardless of time. The reduced trap density has also confirmed the presence of excellent bias stability. Compared to those of the diode with and without the AZO interlayer before the bias stress tests, the forward current value of the diodes with the AZO interlayer after the bias stress test (continuous bias for 3600 s at anode: +3 V, cathode: 0 V) was only changed by 4.4%, and the current value of the diodes without the AZO interlayer decreased significantly by greater than 85.3% (Fig. 4f). When stressed by repeated bias sweeps in ambient air, the device exhibits minimal changes in $J_D - V_D$ characteristics, as shown in Supplementary Fig. 12.

Dynamic response of printed Schottky diode

We also evaluated the high-frequency characteristics of our organic Schottky diodes. Here, the rectifier configuration comprised the diode connected in parallel with a smoothing capacitor and a load resistor. When a sinusoidal input ($V_{in} = 12$ V_{p-p}) was applied, the output voltage decreased as the frequency increased. In contrast to the diode without the interlayer (Fig. 1g), nearly no decrease in the frequency response characteristics was observed in the seven days after air exposure (Fig. 5a). We also found that the frequency characteristics varied depending on the thickness of the semiconductor layer of the diode; however, air stability held regardless of the size of the geometry (Supplementary Fig. 13). The output voltage of the rectifier was approximately 4 V at 13.56 MHz (Fig. 5b). The estimated cutoff frequency (f_c) can be calculated as follows.

$$f_c = \frac{\mu_{SCLC}(V_A - V_{out})}{d^2} \quad (7)$$

Here, μ_{SCLC} is the SCLC carrier mobility, V_A is the applied peak voltage, and d is the semiconductor thickness⁴⁷. The estimate of f_c was approximately 56 MHz (where $V_A = 12$ V, $V_{out} = 5$ V, and $d = 250$ nm) when using a conservatively extracted lower bound estimate of the carrier mobility of DPP-DTT of μ_{SCLC} (5.0×10^{-3} cm²·V⁻¹·s⁻¹), which was extracted by fitting the SCLC $J_D - V_D$ curve. When compared with the field-effect carrier mobility μ_{FET} (4.0×10^{-2} cm²·V⁻¹·s⁻¹) extracted from the transfer curve of the transistor, the μ_{SCLC} was approximately 10 times lower. This discrepancy can be attributed to the fact that carrier transport in the vertical direction of the channel typically occurs at much lower carrier densities than the accumulation of charge density in the channel induced by the gate bias⁴⁸. Compared to the frequency characteristics of organic Schottky diodes based on other solution-processes, the diodes fabricated in this experiment demonstrated superior cutoff frequency performance despite having a thicker OSC film, as shown in Fig. 5c, which depicts the relationship between the cutoff frequency and the thickness of active layer for various carrier mobilities of the semiconductor. The graphs show that the experimental data obtained when changing the thickness of the OSC film are in good agreement with the mobility in 5.0×10^{-3} cm²·V⁻¹·s⁻¹. By utilizing materials with high mobility or forming a uniform ultrathin semiconductor layer that can withstand electrical shorts, polymer organic Schottky diodes can be designed to surpass 13.56 MHz, thereby allowing for utilization in even higher frequency ranges.

Full-wave rectifiers are composed of four organic Schottky diode connections, as shown in Fig. 5d. The active area of the diodes is 2×2 mm² to increase the amount of current. The $J_D - V_D$ characteristics of each of the four diodes and the collectively measured data, when all diodes were connected simultaneously, are shown in Supplementary Fig. 14. By utilizing a 13.56 MHz signal composed of 0101010, it is possible to demonstrate the stability and reproducibility of the organic Schottky diode in the high-frequency regime. This on-off keying modulation signal can be rectified by the organic Schottky diode used in this study to extract the digital information. We confirmed that the rectified signal can be enveloped to obtain a DC signal that contains the original digital information (Fig. 5e). The enveloped signal demonstrates the stable operation of the organic Schottky diode to handle the modulated signals, which may have practical applications in wireless charging and data transmission systems.

Discussion

Due to the printability of solution-processable semiconducting materials, such materials possess numerous benefits, including flexibility, unconventional form factors, customization, large-scale and rapid production, low environmental impact, and seamless integration. Polymers can offer advantages over small molecules while fabricating the active layer of diodes through printing processes. Although small molecules can be utilized for high-speed organic Schottky diodes via physical vapor deposition, their implementation through printing remains challenging because of significant leakage currents and low yield rates (Supplementary Fig. 15). In

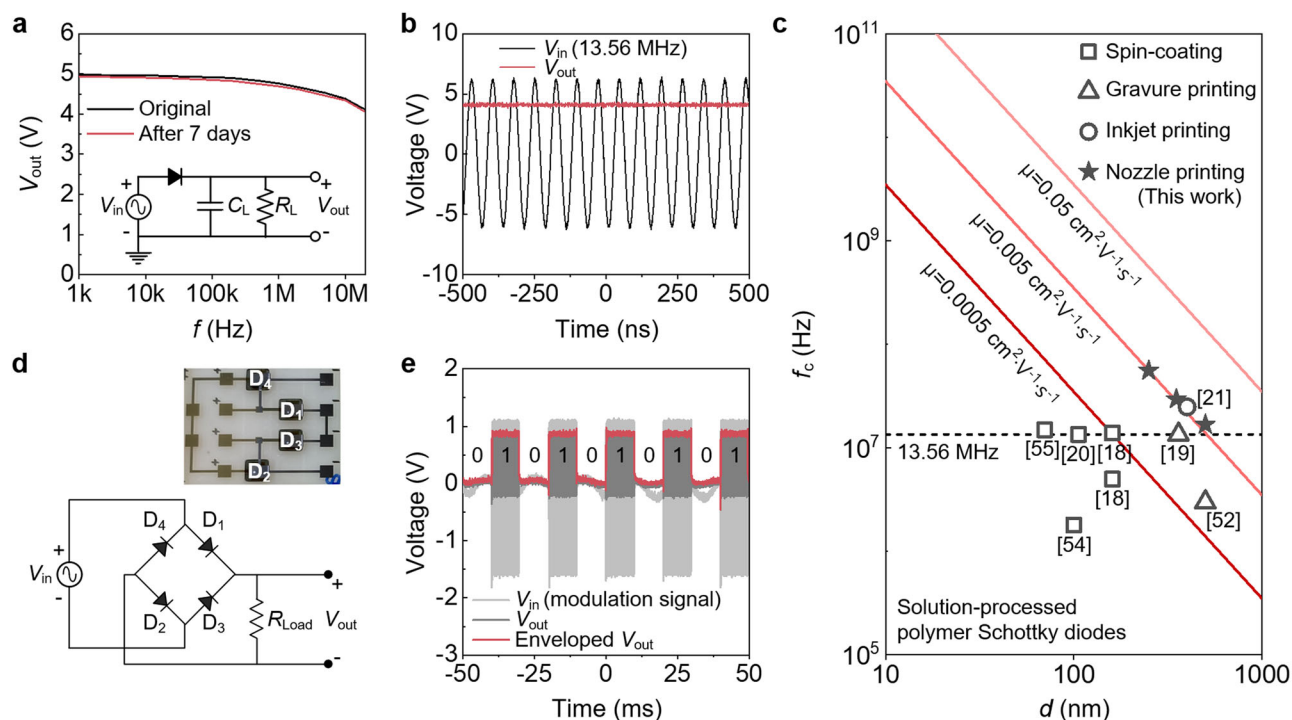


Fig. 5 | Stable full-rectifying operation at 13.56 MHz. **a** Rectified output voltage immediately after fabrication and after 7 days as a function of the frequency of DPP-DTT diode with Al-doped ZnO interlayer. **b** Corresponding full-wave rectified output signal at 13.56 MHz. **c** Cutoff frequency f_c versus diode thickness d for

varying mobility of polymer semiconductor, including performance data from relevant literature for comparison. **d** Full-wave rectifier circuit schematic and optical image of the device. **e** Full-wave envelope detection with 13.56 MHz (010101010) modulation signal.

contrast, polymers exhibit relatively lower leakage current characteristics due to their lesser tendency for crystallization. However, the nonuniformity of printed polymer semiconductor thickness adversely affects the frequency response of polymer diodes. This challenge was overcome by forming diodes with uniform active layers through solvent engineering, considering the boiling points and solubilities of semiconductor solvents (Supplementary Fig. 16). Despite being relatively thicker than films produced via physical vapor deposition, printed polymer films possess excellent flatness in the active layer, enabling polymer diodes to operate at frequencies exceeding the standard 13.56 MHz for RFID systems.

While achieving high performance, the most crucial challenge lies in enhancing the long-term stability of the diodes due to the inherent instability and susceptibility of polymers to specific environmental conditions or interactions with contact metals. Through systematic experiments, we found that diode degradation begins at the polymer-cathode metal interface, and controlling the interface properties is essential for diode stability. The penetration of Al destabilized the crystalline structure of the OSC layer, which resulted in trap formation. Using density functional theory (DFT) calculations, we confirmed that the penetrated Al ions do not undergo chemical reactions with the internal polymer OSC to generate traps (Supplementary Fig. 17). The computational results suggest that the probability of penetrated Al ions or neutral atoms positioning themselves in thermodynamically stable regions within the polymer matrix is statistically rare. In addition, there is a relatively low probability of generating new compounds through electrochemical reactions. The interaction between Al atoms or Al ions and the polymer backbone suggests that rather than forming strong bonds spontaneously within the polymer matrix, they tend to diffuse and position themselves due to entropy-driven diffusion and dynamic factors.

In summary, we have demonstrated a highly stable conjugated polymer Schottky diode that can rectify 13.56 MHz signals for several months without degradation. Our findings highlight the critical instability issue associated with the polymer-cathode metal interface and provide a solution by utilizing a few nanometers of a zinc-oxide interlayer between the conjugated polymer and cathode. This approach eliminates the

nonstoichiometric effect and reduces electrical traps, which helps maintain the charge injection efficiency and achieve remarkable environmental and operational stability. We anticipate that these intrinsically stable organic Schottky diodes will facilitate the development of high-speed wireless communication and future energy harvesting, thereby advancing the IoE in conjunction with telemedicine and personalized diagnosis.

Methods

Material preparation and characterization

All organic Schottky diodes used in this study were fabricated on 125- μm thick polyethylene naphthalate (Teonex PEN, DuPont) films. The substrates were cleaned by ultrasonic baths in acetone, isopropyl alcohol, and deionized water for 10 min each and then dried with nitrogen. To modify the work function of the evaporated Au electrodes by a self-assembled monolayer treatment, pentafluorobenzenethiol (PFBT) was prepared in 30 mM solutions using isopropanol. The work function values for bare gold and PFBT-modified gold are -4.74 eV and -5.25 eV, respectively⁴⁹. For the p-type organic semiconductor (OSC) ink, a hole-transporting polymer, i.e., diketopyrrolo-pyrrole-dithiophene-thienothiophene (DPP-DTT, Ossila), was dissolved in orthodichlorobenzene:chloroform:mesitylene (5:3:2) at a concentration of $5\text{ mg}\cdot\text{ml}^{-1}$. The optimal concentration of DPP-DTT was determined to achieve a high on/off ratio (Supplementary Fig. 18). If the concentration is too low, the semiconductor is too thin, resulting in an electrical short or a large reverse current. In contrast, if the concentration is too high, the current level is too low. A hydrophobic fluoropolymer (Teflon AF1600, DuPont) prepared in a 1 wt% solution using perfluorotributylamine (Fluorinert FC-43, 3 M) as the solvent was used for surface energy modification to define the semiconductor area precisely. An Al-doped zinc-oxide nanoparticle ink (Sigma-Aldrich), which is 2.5 wt% in 2-propanol, was employed for the interlayer between the cathode and the OSC. We used ink that has a -4.3 eV work function to preserve the Schottky contact. For the conformal

deposition of substrates, chemical vapor deposition of a poly(p-xylylene) derivative (Parylene diX-SR, KISCO Ltd.) was used.

The density functional theory (DFT) calculations were performed using the Gaussian 16 package with the long-range-corrected ω B97X-D/6-31G(d,p) method after optimizing the geometry of the model structures.

Device fabrication

To fabricate the organic Schottky diodes, a 300-nm thick parylene film was formed on a 125- μ m thick PEN substrate surface via chemical vapor deposition to achieve good adhesion between the PEN and gold. On the parylene-coated surface, Au electrodes (50-nm thick) as anodes were thermal evaporated at an evaporation rate of $0.1\text{--}0.2\text{ \AA}\cdot\text{s}^{-1}$. For the work function modification of the evaporated Au electrodes using self-assembled monolayer treatment, the sample was dipped into a PFBT solution and then rinsed using isopropyl alcohol. Using a dispenser printer (Image Master 350PC, Musashi Engineering), a hydrophobic fluoropolymer, i.e., Teflon, was printed along the rectangular outlines of the diode active areas to store OSC ink. A p-type semiconductor DPP-DTT ink was printed using a dispenser to fill the inside of the Teflon bank area, and then the film was annealed at $100\text{ }^{\circ}\text{C}$ for 30 minutes. Note that the semiconductor printing was conducted in an ambient environment. The direction of the printing process was square clockwise (from the inside to the outside) to fill the ink as evenly as possible. The active channels for fabricating organic field-effect transistors were printed in a straight line, with further details that can be found in our previous work^{50,51}. The Teflon bank was dissolved and removed through its solvent, i.e., FC-43, for the subsequent spin-coating process. The AZO ink was spin-coated at 5000 rpm for 1 minute and then annealed at $100\text{ }^{\circ}\text{C}$ for 10 minutes. Finally, on the AZO layer, Al electrodes (100-nm thick) as cathodes were thermal evaporated at an evaporation rate of $5\text{--}6\text{ \AA}\cdot\text{s}^{-1}$. The device area was $1000 \times 1000\text{ }\mu\text{m}^2$.

Device characterization

The $J_D\text{--}V_D$ and $C\text{--}V_D$ characteristic measurements of the diodes were conducted in an ambient air environment using a semiconductor parameter analyzer (Keithley, 4200-SCS). The electrical characteristics of the diodes were compared with those of other solution-processed organic semiconductor-based Schottky diodes (Supplementary Table 1)^{18–21,52–58}. In addition, a stylus profiler (Dektak XT, Bruker) was used to measure the thickness and roughness of the thin films. The dielectric constant of the DPP-DTT p-type semiconductor was measured using an LCR meter (NF Corporation, ZM2376), and the surface chemistry of the interface between the Al and OSC was analyzed using an X-ray photoelectron spectrometer system (XPS) (K-Alpha, Thermo Fisher Scientific) and secondary ion mass spectroscopy (SIMS) (IMS 6 F, CAMECA). The cross-section image of the device structure was obtained by field emission scanning electron microscopy (JSM 7401F, JEOL).

Data availability

The data that support the findings of this study are available from Y.L., S.J., and J.K. on reasonable request.

Received: 19 March 2024; Accepted: 28 June 2024;

Published online: 18 July 2024

References

- Someya, T., Bao, Z. & Malliaras, G. G. The rise of plastic bioelectronics. *Nature* **540**, 379–385 (2016).
- Lee, G. H. et al. Multifunctional materials for implantable and wearable photonic healthcare devices. *Nat. Rev. Mater.* **5**, 149–165 (2020).
- Baek, S. et al. Spatiotemporal measurement of arterial pulse waves enabled by wearable active-matrix pressure sensor arrays. *ACS Nano* **16**, 368–377 (2022).
- Zhang, Z. et al. High-brightness all-polymer stretchable LED with charge-trapping dilution. *Nature* **603**, 624–630 (2022).
- Koo, J. H., Kim, D. C., Shim, H. J., Kim, T. H. & Kim, D. H. Flexible and stretchable smart display: materials, fabrication, device design, and system integration. *Adv. Funct. Mater.* **28**, 1801834 (2018).
- Gao, W. et al. Fully integrated wearable sensor arrays for multiplexed in situ perspiration analysis. *Nature* **529**, 509–514 (2016).
- Wang, S. et al. Skin electronics from scalable fabrication of an intrinsically stretchable transistor array. *Nature* **555**, 83–88 (2018).
- You, I. et al. Artificial multimodal receptors based on ion relaxation dynamics. *Science* **370**, 961–965 (2020).
- Cea, C. et al. Enhancement-mode ion-based transistor as a comprehensive interface and real-time processing unit for in vivo electrophysiology. *Nat. Mater.* **19**, 679–686 (2020).
- Lee, Y. et al. Tunable organic active neural probe enabling near-sensor signal processing. *Adv. Mater.* **35**, 1–11 (2023).
- Chu, Y., Qian, C., Chahal, P. & Cao, C. Printed diodes: materials processing, fabrication, and applications. *Adv. Sci.* **6**, 1801653 (2019).
- Zhong, D. et al. High-speed and large-scale intrinsically stretchable integrated circuits. *Nature* **627**, 313–320 (2024).
- Myny, K. The development of flexible integrated circuits based on thin-film transistors. *Nat. Electron.* **1**, 30–39 (2018).
- Kwon, J. et al. Three-dimensional monolithic integration in flexible printed organic transistors. *Nat. Commun.* **10**, 54 (2019).
- Kim, W., Kwon, J., Lee, Y., Baek, S. & Jung, S. Phase-separated, printed organic thin-film transistor-based nonvolatile memory with enhanced data retention. *Adv. Mater. Technol.* **5**, 1–5 (2020).
- Kwon, J., Lee, Y., Jo, Y. & Jung, S. Fabrication of ultrathin low-voltage-driven printed organic circuits with anodized gate islands. *Org. Electron. Phys., Mater. Appl.* **62**, 77–81 (2018).
- Kwon, J., Jung, S., Baek, S., Lee, Y. & Tokito, S. Layout-to-bitmap conversion and design rules for inkjet-printed large-scale integrated circuits. *Langmuir* **37**, 10692–10701 (2021).
- Lin, C. Y. et al. High-frequency polymer diode rectifiers for flexible wireless power-transmission sheets. *Org. Electron.* **12**, 1777–1782 (2011).
- Heljo, P. S., Li, M., Lilja, K. E., Majumdar, H. S. & Lupo, D. Printed half-wave and full-wave rectifier circuits based on organic diodes. *IEEE Trans. Electron Devices* **60**, 870–874 (2013).
- Higgins, S. G., Agostinelli, T., Markham, S., Whiteman, R. & Sirringhaus, H. Organic diode rectifiers based on a high-performance conjugated polymer for a near-field energy-harvesting circuit. *Adv. Mater.* **29**, 1–6 (2017).
- Viola, F. A. et al. A 13.56 MHz rectifier based on fully inkjet printed organic diodes. *Adv. Mater.* **32**, 1–7 (2020).
- Matsuhisa, N. et al. High-frequency and intrinsically stretchable polymer diodes. *Nature* **600**, 246–252 (2021).
- Nikolka, M. et al. High operational and environmental stability of high-mobility conjugated polymer field-effect transistors through the use of molecular additives. *Nat. Mater.* **16**, 356–362 (2017).
- Hasegawa, F., Onomura, M., Mogi, C. & Nannichi, Y. Reduction of Schottky barrier heights by surface oxidation of GaAs and its influence on DLTS signals for the midgap level EL2. *Solid State Electron* **31**, 223–228 (1988).
- Nithya, P. M. & Devi, L. G. Effect of surface Ag metallization on the photocatalytic properties of BaTiO₃: Surface plasmon effect and variation in the Schottky barrier height. *Surf. Interfaces* **15**, 205–215 (2019).
- Nikolka, M. et al. High-mobility, trap-free charge transport in conjugated polymer diodes. *Nat. Commun.* **10**, 1–9 (2019).
- Lu, Q. et al. A review on encapsulation technology from organic light emitting diodes to organic and perovskite solar cells. *Adv. Funct. Mater.* **31**, 2100151 (2021).
- Iqbal, H. F. et al. Suppressing bias stress degradation in high performance solution processed organic transistors operating in air. *Nat. Commun.* **12**, 1–10 (2021).

29. Chiba, T., Pu, Y.-J. & Kido, J. Low Molecular Weight Materials: Electron Injection Materials. *Handb. Org. Light. Diodes* 1–8 (2021) https://doi.org/10.1007/978-4-431-55761-6_7-1.
30. Yang, J., Zhao, Z., Wang, S., Guo, Y. & Liu, Y. Insight into high-performance conjugated polymers for organic field-effect transistors. *Chem* **4**, 2748–2785 (2018).
31. Dong, H., Wang, C. & Hu, W. High performance organic semiconductors for field-effect transistors. *Chem. Commun.* **46**, 5211–5222 (2010).
32. da Cunha, M. R. P., Maciel, A. C., Faria, R. M. & da Cunha, H. N. Differential capacitive response of poly (3-hexylthiophene) diodes and effects of air exposure. *Synth. Met.* **253**, 141–145 (2019).
33. Matsuhisa, N. et al. A mechanically durable and flexible organic rectifying diode with a Polyethylenimine ethoxylated cathode. *Adv. Electron. Mater.* **2**, 2–9 (2016).
34. Li, Y., Minari, T., Kumatani, A., Tsukagoshi, K. & Darmawan, P. On practical charge injection at the metal/organic semiconductor interface. *Sci. Rep.* **3**, 3–8 (2013).
35. Li, Y., Singh, S. P. & Sonar, P. A high mobility P-type DPP-thieno[3,2-b]thiophene copolymer for organic thin-film transistors. *Adv. Mater.* **22**, 4862–4866 (2010).
36. Li, J. et al. A stable solution-processed polymer semiconductor with record high-mobility for printed transistors. *Sci. Rep.* **2**, 1–9 (2012).
37. Fladischer, S. et al. Diffusion of Ag into organic semiconducting materials: A combined analytical study using transmission electron microscopy and X-ray reflectivity. *ACS Appl. Mater. Interfaces* **4**, 5608–5612 (2012).
38. Rujisamphan, N., Tang, I. M., Sutthibutpong, T., Amornkitbamrung, V. & Supasai, T. Revealing the diffusion of aluminum in organic solar cells. *Jpn. J. Appl. Phys.* **58**, 050904 (2019).
39. Faupel, F., Zaporozhchenko, V., Thran, A., Strunskus, T. & Kiene, M. Metal Diffusion in Polymers and on Polymer Surfaces. In *Diffusion Processes in Advanced Technological Materials* 333–363 (2005). <https://doi.org/10.1016/B978-081551501-2.50009-5>.
40. Idriss, H. On the wrong assignment of the XPS O1s signal at 531–532 eV attributed to oxygen vacancies in photo- and electro-catalysts for water splitting and other materials applications. *Surf. Sci.* **712**, 2–7 (2021).
41. Gupta, R. K. & Singh, R. A. Schottky diode based on composite organic semiconductors. *Mater. Sci. Semicond. Process.* **7**, 83–87 (2004).
42. Mott, N. F.; Gurney, R. W. Electronic Processes in Ionic Crystals. *Oxford Univ. Press* (1940).
43. Gelderman, K., Lee, L. & Donne, S. W. Flat-band potential of a semiconductor: Using the Mott-Schottky equation. *J. Chem. Educ.* **84**, 685–688 (2007).
44. Campbell, A. J., Bradley, D. D. C., Werner, E. & Brütting, W. Deep level transient spectroscopy (DLTS) of a poly(p-phenylene vinylene) Schottky diode. *Synth. Met.* **111**, 273–276 (2000).
45. Heath, J. T., Cohen, J. D. & Shafarman, W. N. Bulk and metastable defects in CuIn1-xGaxSe2 thin films using drive-level capacitance profiling. *J. Appl. Phys.* **95**, 1000–1010 (2004).
46. Li, J. V. et al. Simultaneous measurement of carrier density and mobility of organic semiconductors using capacitance techniques. *Org. Electron.* **12**, 1879–1885 (2011).
47. Steudel, S. et al. 50 MHz rectifier based on an organic diode. *Nat. Mater.* **4**, 597–600 (2005).
48. Trukhanov, V. A., Bruevich, V. V. & Paraschuk, D. Y. Effect of space charge limited current on performance of organic field-effect transistors. *Synth. Met.* **246**, 254–259 (2018).
49. Marmont, P. et al. Improving charge injection in organic thin-film transistors with thiol-based self-assembled monolayers. *Org. Electron.* **9**, 419–424 (2008).
50. Lee, Y. et al. Reliable inkjet contact metallization on printed polymer semiconductors for fabricating staggered TFTs. *Appl. Phys. Lett.* **116**, (2020).
51. Lee, Y., Kwon, J., Kim, W. & Jung, S. Flexible printed top-contact organic thin-film transistors. *2019 IEEE Int. Flex. Electron. Technol. Conf.* 1–1 (2019) <https://doi.org/10.1109/IFETC46817.2019.9073708>.
52. Lilja, K. E., Bäcklund, T. G., Lupo, D., Hassinen, T. & Joutsenoja, T. Gravure printed organic rectifying diodes operating at high frequencies. *Org. Electron.* **10**, 1011–1014 (2009).
53. Ng, T. N. et al. Pulsed voltage multiplier based on printed organic devices. *Flex. Print. Electron.* **1**, 015002 (2016).
54. Kim, K. D. et al. Variations in the electric characteristics of an organic schottky diode with the P3HT thickness. *J. Korean Phys. Soc.* **57**, 124–127 (2010).
55. Altazin, S. et al. Physics of the frequency response of rectifying organic Schottky diodes. *J. Appl. Phys.* **115**, 064509 (2014).
56. Bose, I., Tetzner, K., Börner, K. & Bock, K. Air-stable, high current density, solution-processable, amorphous organic rectifying diodes (ORDs) for low-cost fabrication of flexible passive low frequency RFID tags. *Microelectron. Reliab.* **54**, 1643–1647 (2014).
57. Semple, J. et al. Large-area plastic nanogap electronics enabled by adhesion lithography. *npj Flex. Electron.* **2**, 1–10 (2018).
58. Ma, L., Ouyang, J. & Yang, Y. High-speed and high-current density C 60 diodes. *Appl. Phys. Lett.* **84**, 4786–4788 (2004).

Acknowledgements

This work was supported by the National R&D Program through the National Research Foundation of Korea(NRF), funded by the Ministry of Science and ICT (RS-2023-00281195, RS-2023-00258309, RS-2024-00355384), the National Research Foundation (NRF), Korea, under project BK21 FOUR, and the Korea Innovation Foundation (INNOPOLIS) grant (2020-DD-UP-0278) funded by the Korea government (MSIT).

Author contributions

Y.L., S.J., and J.K. conceived the project. Y.L. and J.K. designed the experiments. Y.L. performed experiments on device fabrication. Y.L., B.K., S.J., and J.K. analyzed the experimental data and discussed the results. B.K. contributed to the analysis of DFT calculation. S.J. and J.K. supervised the project. The manuscript was written by Y.L., B.K., S.J., and J.K. in close consultation with the other authors.

Competing interests

All authors declare no competing interests.

Additional information

Supplementary information The online version contains supplementary material available at <https://doi.org/10.1038/s41528-024-00326-y>.

Correspondence and requests for materials should be addressed to Sungjune Jung or Jimin Kwon.

Reprints and permissions information is available at <http://www.nature.com/reprints>

Publisher's note Springer Nature remains neutral with regard to jurisdictional claims in published maps and institutional affiliations.

Open Access This article is licensed under a Creative Commons Attribution 4.0 International License, which permits use, sharing, adaptation, distribution and reproduction in any medium or format, as long as you give appropriate credit to the original author(s) and the source, provide a link to the Creative Commons licence, and indicate if changes were made. The images or other third party material in this article are included in the article's Creative Commons licence, unless indicated otherwise in a credit line to the material. If material is not included in the article's Creative Commons licence and your intended use is not permitted by statutory regulation or exceeds the permitted use, you will need to obtain permission directly from the copyright holder. To view a copy of this licence, visit <http://creativecommons.org/licenses/by/4.0/>.

© The Author(s) 2024